Electronic Supplementary Material (ESI) for Nanoscale.

Supporting Information

Direct visualization of fluid dynamics in sub-10 nm nanochannels

Huawei Li,[†,††] Junjie Zhong,[†] Yuanjie Pang,[†] Seyed Hadi Zandavi,[†] Aaron Harrinarine Persad,[†] Yi Xu,[†] Farshid Mostowfi,[‡] and David Sinton[†,*]

[†] Department of Mechanical and Industrial Engineering, University of Toronto, M5S 3G8 Canada

[††] School of Electromechanical Engineering, Guangdong University of Technology, Guangzhou, 510006 China

[‡] Schlumberger-Doll Research, Cambridge, Massachusetts, 02139 USA

[*] corresponding author: sinton@mie.utoronto.ca

Section 1: Finite-difference time-domain (FDTD) simulations

Section 2: Sub-10 nm nanofluidic chip fabrication procedure

Section 3: Survivability of sub-10 nm high nanochannels during anodic bonding process

Section 4: Capillary filling in sub-10 nm high nanochannels

Section 5: Error analysis for capillary filling

Section 6: Capillary filling video

Section 7: Debye length calculations for salt concentrations

Section 1: Finite-difference time-domain (FDTD) simulations

In order to examine and understand the effect of the Si_3N_4 layer on the contrast enhancement between the liquid and gas phases in the 8-nm high channels, finite-difference time-domain (FDTD) simulations were performed using a commercially available computational electromagnetic software package (Lumerical FDTD). Figure S1 shows the reflective spectrum from the gas-filled (*e.g.*, air) channels, the liquid-filled (*e.g.*, water) channels, and the wall (the bonded area) in the glass-silicon nanofluidic chip (a) without and (c) with the Si_3N_4 layer. In case (c), reflectivity from the SiO_2-Si_3N_4 interface of the nanofluidic chip exhibits a distinct peak-valley feature resulting from the Fabry-Perot optical cavity formed by the Si_3N_4 layer and the nanochannel. When there is a gas-filled or liquid-filled nanochannel above the Si_3N_4 layer, tiny perturbations in the refractive index are introduced to the Fabry-Perot cavity, resulting in a finite shift of the spectrum, depending on the difference in refractive index between the cover glass and the substance (*i.e.*, gas or liquid) in the channel. In comparison, the reflected spectrum from the nanochannel without the Si_3N_4 layer is relatively flat and cannot sense the refractive index change.

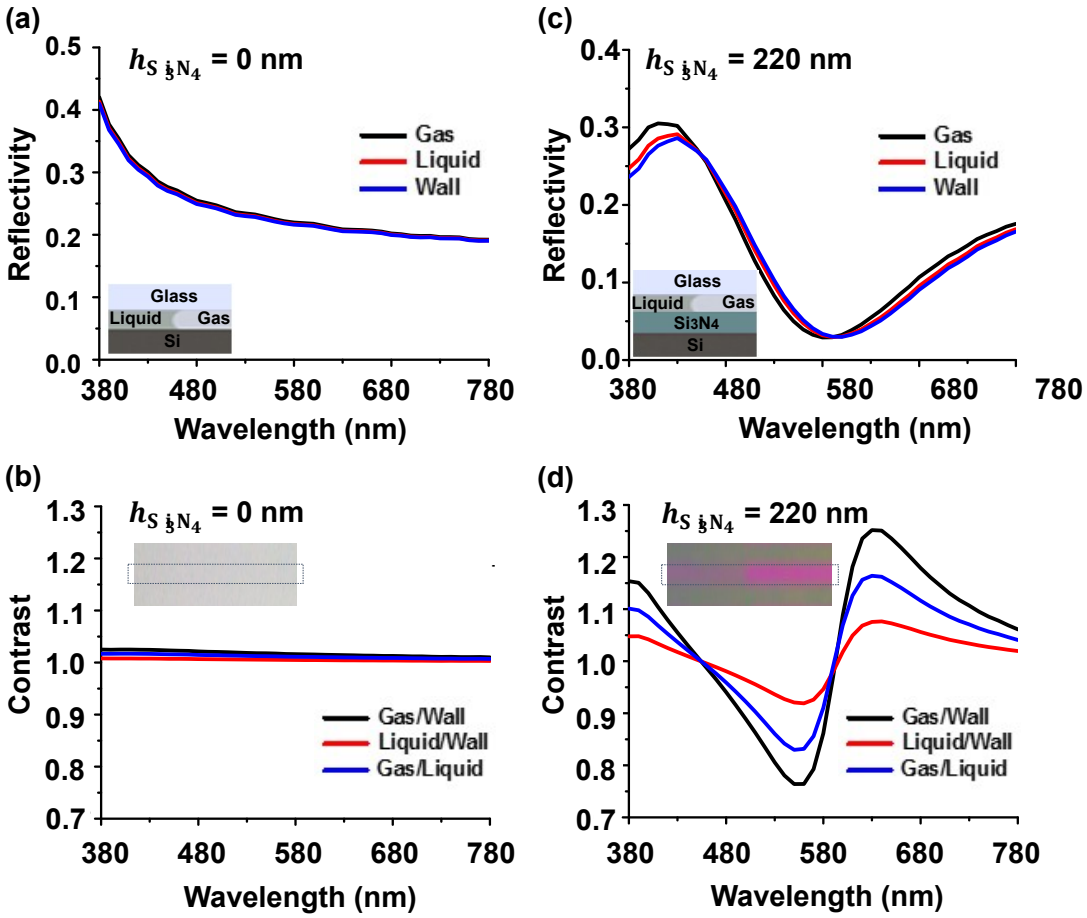

Figure S1. FDTD simulation results of reflectivity and contrast spectra for an 8-nm high channel without (a, b) and with (c, d) the Si_3N_4 layer.

To measure the visibility of different substances, we define the image contrast as the ratio of reflectivity between the substance (*i.e.*, liquid or gas) and the wall. As plotted in Figure S1d, the contrasts of both the gas and liquid against the wall are significantly different from unity at any wavelength of visible light, thus ensuring the visibility of gas and liquid in the channel. Importantly, the contrast of gas to wall is greater than that of the liquid to the wall, which allows discrimination between liquid and gas phases. In contrast, for conventional chips without the Si_3N_4 layer, the simulation results (Figure S1c) show that both the gas-filled and the liquid-filled nanochannels are difficult to distinguish from the wall (*i.e.*, the contrast is very close to unity over the full wavelength range of visible light). Thus, without the Si_3N_4 layer, visualization of fluid dynamics at sub-10 nm scale is expected to be very difficult.

FDTD simulations were performed to verify the dependence of gas/liquid contrast on the thickness of the Si_3N_4 layer, and the results for thicknesses of 100, 150, 220 and 400 nm are shown in Figure S2. For the Si_3N_4 layer thicknesses of 100, 150 and 220 nm, the contrasts between gas and liquid in the 8-nm high nanochannels are well enhanced, but not as impressive in the 400 nm case.

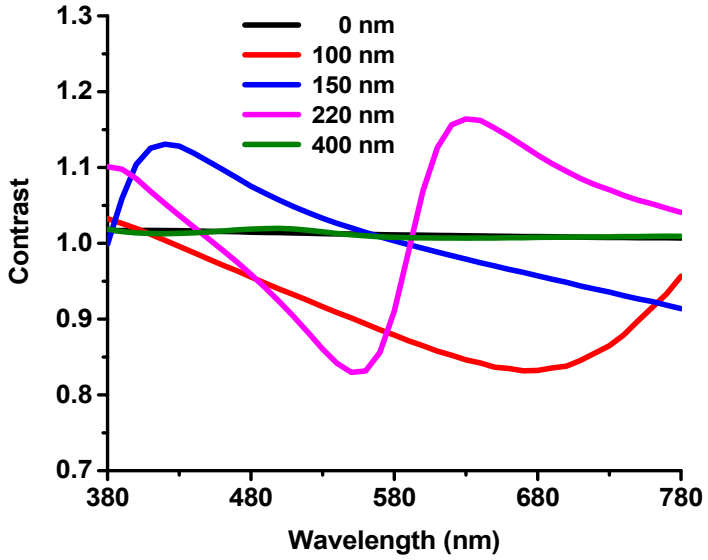

Figure S2. Dependence of gas/liquid contrast on the thickness of the Si_3N_4 layer.

Section 2: Sub-10 nm nanofluidic chip fabrication procedure

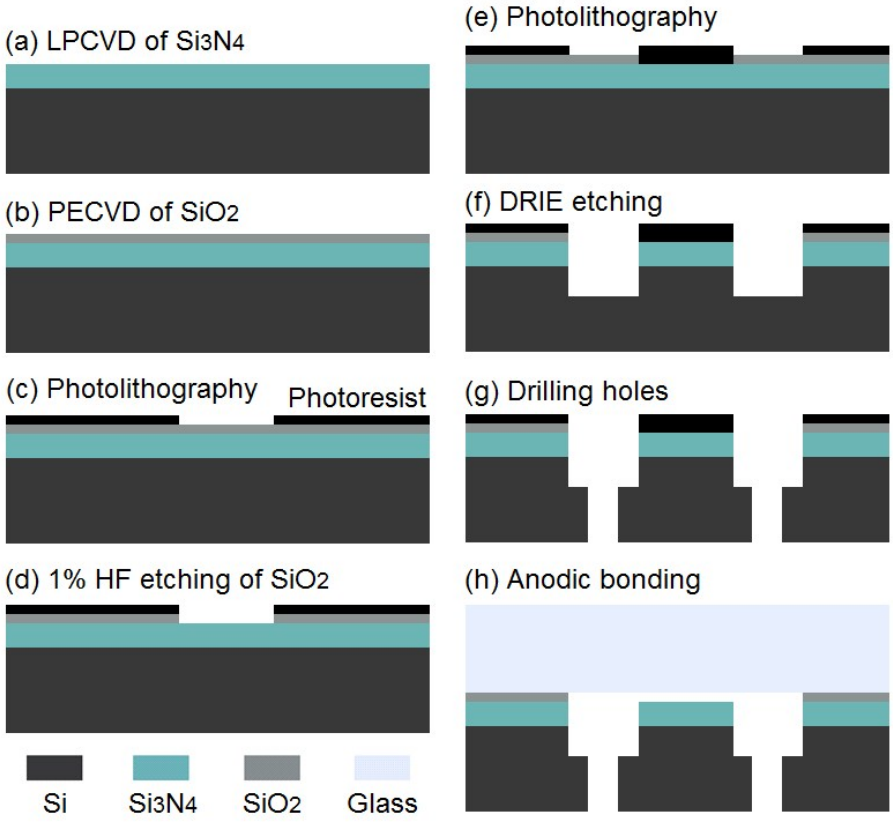

Figure S3. Nanofluidic chip fabrication procedure: (a) a Si_3N_4 layer is grown on a 1-mm thick single side polished silicon wafer by LPCVD (low pressure chemical vapor deposition); (b) a SiO_2 layer with a thickness down to a few nanometers (8 nm thick in this study) was grown on top of the Si_3N_4 layer by PECVD (plasma enhanced chemical vapor deposition); (c) Photolithography for nanochannels; (d) Selective etching of SiO_2 by dilute HF; (e) Photolithography for microchannels (100-μm wide); (f) DRIE etching for microchannels (50-μm high); (g) Drilling inlet and outlet holes; (h) Anodic bonding between glass and silicon chip after piranha cleaning (600 V and 4 mA for 1 minute, at a temperature of 400 °C, atmospheric pressure of 10^{-3} Pa, and an applied force of $1.3x10^4$ Pa).

Section 3: Survivability of sub-10 nm nanochannels during anodic bonding process

Figure S4 shows the schematics of the anodic bonding process and the equivalent electronic circuits. Traditional anodic bonding of glass and Si wafer, as shown in Figure S4a, has a minimum channel height, h_{min}, that is able to survive collapse for a given channel width, w: [1]

$$h_{min} = V_{channel}^{2/3} \cdot \sqrt[3]{w\varepsilon_0\left[\frac{\left(1-v_{Si}^2\right)}{E_{Si}} + \frac{\left(1-v_g^2\right)}{E_g}\right]} \quad \text{(S1)}$$

where $\mathcal{E}_0$ is the permittivity of the vacuum, $V_{channel}$ is the voltage drop across the channel, V_{si} and V_g are the Poisson's ratio for silicon wafer and the borofloat glass, respectively, and E_{si} and E_g are the Yong's modulus for the silicon wafer and the borofloat glass at the bonding temperature, respectively.

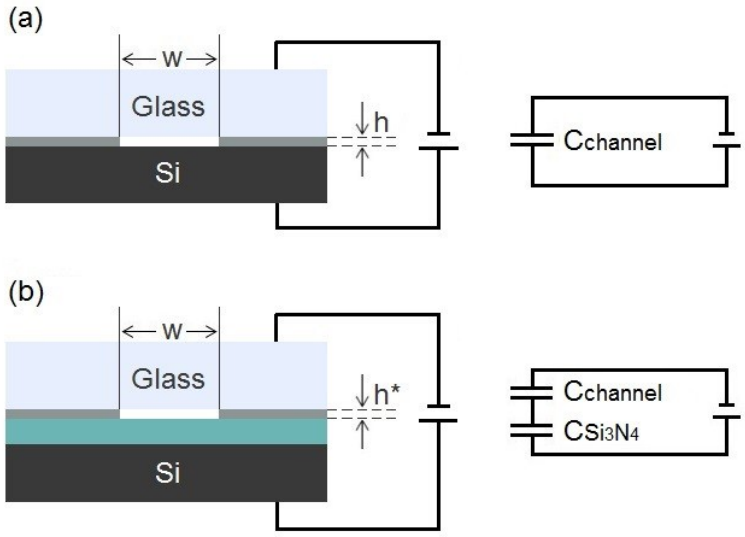

Figure S4. Schematics of the equivalent electronic circuits during the anodic bonding process. (a) Traditional anodic bonding with its equivalent electronic circuit; (b) Anodic bonding with the Si_3N_4 layer and its equivalent electronic circuit.

For the traditional anodic bonding, $v_{channel}$ can be assumed to be equal to the total applied voltage, resulting in

$$h_{min} = v_{total}^{2/3} \cdot \sqrt[3]{w\varepsilon_0\left[\frac{\left(1-v_{Si}^2\right)}{E_{Si}} + \frac{\left(1-v_g^2\right)}{E_g}\right]} \quad \text{(S2)}$$

Therefore, channel collapse during anodic bonding process can be avoided if $h \geq h_{min}$. In our tests, using 400 ℃, 600 V and 1 A anodic bonding condition, the minimum height to avoid channel collapse in 4-μm wide nanochannels is 16 nm (limit of aspect ratio = 0.004);[2] nanochannels shallower than 16 nm are expected to collapse.

For the anodic bonding with the dielectric Si_3N_4 layer under the nanochannel, the layer serves as a series capacitor that satisfies the equation[1]

$$C_{channel} v_{channel}^{*} = C_{Si_3N_4} v_{Si_3N_4} \quad \text{(S3)}$$

$$v_{total} = v_{channel}^{*} + v_{Si_3N_4} \quad \text{(S4)}$$

where $C_{channel}$ and $C_{Si_3N_4}$ are the capacitance of the nanochannel and the Si_3N_4 layer, respectively, and $v_{channel}^{*}$ and $v_{Si_3N_4}$ are the voltage drops across the nanochannel and the Si_3N_4 layer, respectively. $C_{channel}$ and $C_{Si_3N_4}$ can be further expressed as

$$C_{channel} = \varepsilon_0 \frac{wL}{h} \quad \text{(S5)}$$

and

$$C_{Si_3N_4} = \varepsilon_0 \varepsilon_{Si_3N_4} \frac{wL}{d_{Si_3N_4}} \quad \text{(S6)}$$

where L is the channel length, $\varepsilon_{Si_3N_4}$ is the relative dielectric constant of Si_3N_4, and $d_{Si_3N_4}$ is the thickness of the Si_3N_4 layer. $v_{channel}^{*}$ is then calculated from equation

$$\frac{v_{channel}^{*}}{\frac{h}{\varepsilon_0}} = \frac{v_{Si_3N_4}}{\frac{d_{Si_3N_4}}{\varepsilon_0 \varepsilon_{Si_3N_4}}} = \frac{v_{channel}^{*} + v_{Si_3N_4}}{\frac{h}{\varepsilon_0} + \frac{d_{Si_3N_4}}{\varepsilon_0 \varepsilon_{Si_3N_4}}} = \frac{v_{total}}{\frac{h}{\varepsilon_0} + \frac{d_{Si_3N_4}}{\varepsilon_0 \varepsilon_{Si_3N_4}}} \quad \text{(S7)}$$

so that

$$v_{channel}^{*} = \frac{\frac{h}{\varepsilon_0} v_{total}}{\frac{h}{\varepsilon_0} + \frac{d_{Si_3N_4}}{\varepsilon_0 \varepsilon_{Si_3N_4}}} \quad \text{(S8)}$$

In the case of $h << d_{Si_3N_4}$, equation (S8) can be further simplified as

$$v_{channel}^{*} = \frac{h \varepsilon_{Si_3N_4}}{d_{Si_3N_4}} v_{total} \quad \text{(S9)}$$

Substituting equation (S9) into equation (S1), the minimum channel height h_{min}^{*} for the anodic bonding with the Si_3N_4 layer can be expressed as

$$h_{min}^{*} = \left(\frac{h_{min}^{*}\varepsilon_{Si_3N_4}}{d_{Si_3N_4}}\right)^{2}/_{3} \cdot v_{total}^{\ 2}/_{3} \cdot \sqrt[3]{w\varepsilon_0\left[\frac{\left(1-v_{Si}^2\right)}{E_{Si}} + \frac{\left(1-v_g^2\right)}{E_g}\right]} \quad \text{(S10)}$$

Substituting equation (S2) into equation (S10), h_{min}^{*} can be further simplified as

$$h_{min}^{*} = \left(\frac{\varepsilon_{Si_3N_4}}{d_{Si_3N_4}}\right)^2 \cdot h_{min}^{\ 3} \quad \text{(S11)}$$

For 220-nm thick Si_3N_4 layer in our study, considering that h_{min} = 16 nm for 4-μm wide nanochannels, h_{min}^{*}= 4.76 nm, so that the survivability of 8-nm high nanochannels during anodic bonding process are guaranteed.

Section 4: Capillary filling in sub-10 nm high nanochannels

Experimental procedure

A total of 200 capillary filling arrays (each array consists of 5 parallel nanochannels, see Figure 4a) were fabricated on a single chip. Before each experiment, the chip was heated to 400 ℃ and evacuated for 3 hours to prevent formation of bubbles and contamination in the nanochannels. Afterward, tape was used to block the inlet and outlet holes of each array. The chip was mounted onto a bright-field inverted Olympus microscope. The tape over one of the arrays was removed and a droplet of 5 μL of the test liquid was deposited onto the exposed inlet hole of the microchannel by pipetting so that both the microchannel and the nanochannels connected to the microchannel could be filled by capillary action. The position of the moving meniscus (liquid-air interface) was tracked and recorded as a function of time by a camera (frame rate = 20 s^{-1}) that was mounted to the microscope. After the nanochannel filling video was recorded, the remaining droplet was wiped away and another array was exposed (inlet and outlet) to another run. The liquid column length and the liquid-air interface positions were extracted from the videos using a MATLAB image processing code. The hydrocarbons (hexane, octane and hexadecane) were pure (>99.5%) and used from the supplier bottle (Sigma) without additional processing. De-ionized water was obtained from the Centre for Microfluidic Systems in Chemistry and Biology and had a resistivity of 18.2 MΩcm. To study the electric double layer (EDL) effect, we prepared sodium chloride solutions with concentrations of 0.1 M and 1.0 M (NaCl, Bioshop, Reagent Grade, >99.0%).

Fluid Properties

Fluid properties are listed in Table S1 below. The static contact angles of the liquids were measured on bare silicon wafers, wafers coated with Si_3N_4, and on borosilicate glass (the chip glass cover). All liquids had a contact angle of approximately 0° on Si_3N_4, *i.e.*, they were completely wetting. Only water and the NaCl aqueous solutions had non-zero contact angles on borosilicate glass, as indicated in Table S1. Our measured contact angle agrees with that reported in the literature: the contact angle of water on untreated borosilicate glass at 22 °C was reported to be 32 ± 2°.[5] When it is assumed that the classical Lucas-Washburn equation is correct, the *dynamic* contact angle is treated as a fitting parameter and the value for water on SiO_2 was calculated to be 68° in 50-nm

high channels.[6] Similarly, the dynamic contact angle of water on Pyrex glass was 68 ± 12°.[7] The question of which contact angle to use (static or dynamic) in the Lucas-Washburn equation remains open. Oyarzua *et al.* used the static contact angle in their approach.[8] Their contact angle of water on silica was 15°, and they calculated an initial dynamic value of 80° in a 6-nm high channel.

In the calculations that follow, we also use the static contact angle values on borosilicate glass (see Table S1) since they provide a conservative estimate on the values of C_V and t_I in eqn S14.

Table S1. Physical properties of liquids at 20 ± 1°C. Bracketed errors are due to the temperature uncertainty.

Test liquid	Liquid-air surface tension[b], γ (mN/m)	Liquid viscosity[b], μ (mPa·s)	Contact angle[a] on borosilicate glass, θ (°)	Contact angle[a] on silicon, θ (°)	Contact angle[a] on silicon nitride, θ (°)	Dipole moments, D_p (D)	Molar mass, M_W (g/mol)
Hexane	18.5 (± 0.1)[d]	0.30 (± 0.08)[d]	<5	<5	<5	0	86.18
Octane	21.6 (± 0.1)	0.54 (± 0.01)	<5	<5	<5	0	114.23
Hexadecane	27.5 (± 0.1)[c]	3.50 (± 0.08)[c]	<5	<5	<5	0	223.45
Water	73.7 (± 0.2)	1.02 (± 0.05)	33 ± 5	40 ± 5	23 ± 5	1.85	18.02
NaCl 0.1 M	73.9 (± 0.2)[d]	1.01 (± 0.05)[e]	36 ± 5	45 ± 5	26 ± 5	---	18.07[f]
NaCl 1.0 M	75.3 (± 0.2)[d]	1.09 (± 0.05)[e]	41 ± 5	49 ± 5	27 ± 5	---	18.73[f]

[a] Measured under the lab atmosphere (25-40% relative humidity)
[b] Fluid properties reported by the Data Institute for Physical Properties Research (DIPPR)[3]
[c] Fluid properties reported by Yaws[4]
[d] Fluid properties reported by the National Physics Laboratory (NPL)[18]
[e] Fluid properties reported by Kestin *et al*. [19]
[f] Average molar mass

Modified Lucas-Washburn equation

As described in the main manuscript, a modified Lucas-Washburn relation is used to model the capillary filling data:

$$x(t) = \sqrt{\frac{\gamma \cos\theta h t}{3C_V \mu}} + C_I(t_I) \qquad \text{(S12)}$$

In eqn S12, the C_V terms accounts for viscous effects in nanoconfinement while the $C_I(t_I)$ term accounts for inertial effects at the nanochannel entrance. The time it takes for the flow to follow an *x vs.* $\sqrt{t}$ behavior is denoted by t_I. Several functional forms of $C_I(t_I)$ exist, such that used in Bosanquet equation.[8] However, for simplicity, we consider the form:

$$C_I(t_I) = \sqrt{\frac{\gamma \cos\theta h t_I}{3C_V \mu}} \qquad \text{(S13)}$$

In eqn S13, t_I delays the onset of the viscous-dominated flow regime. By using eqn S13, we can express eqn S12 as:

$$x(t) = \sqrt{\frac{\gamma \cos\theta h}{3C_V \mu}}\left(\sqrt{t} - \sqrt{t_I}\right) \qquad \text{(S14)}$$

There are two fitting parameters in eqn S14, C_V and t_I, and these were determined using the NonLinearFit function in Mathematica 11 with the filling video data and the fluid properties listed in Table S1. The values of C_V and t_I are listed in Table S2. The values of $t_I$were determined by comparing the filling data to the model, eqn S14. The time where the model and data start to converge is taken to be t_I, and the values are listed in Table S2.

Some trends can be identified in Table S2 when we compare the hydrocarbons against each other. The values of t_I increase with molecular weight. Also note that the t_I value of hexane is three times smaller than that of hexadecane, even though their C_V values are similar (1.20 and 1.24, respectively). These results could be interpreted to indicate that heavier molecules take longer to follow a viscous-dominated flow, consistent with the observations reported by Elton *et al.* who claim that inertial effects on the capillary flow can be dominant at the nanochannel's entrance.[8]

Table S2. Modified Lucas-Washburn equation parameters (eqn S14)

Test liquid	$\sqrt{\frac{\gamma h cos\theta}{3\mu}}$ ($\mu m/s^{0.5}$)	C_V [a]	t_I [b] (s)
Hexane	405.88	1.20 (± 13%)	0.05 (± 10%)
Octane	327.02	1.05 (± 15%)	0.10 (± 8%)
Hexadecane	144.80	1.24 (± 11%)	0.15 (± 2%)
Water	408.10	0.80 (± 20%)	0.53 (± 12%)
NaCl 0.1 M	397.10	1.03 (± 18%)	0.04 (± 32%)
NaCl 1.0 M	372.87	0.78 (± 30%)	0.09 (± 32%)

[a] Uncertainties from error analysis described below

[b] Determined from plots of x vs. $\sqrt{t}$

Other physical interpretations may be assigned to the parameters C_V and t_I, such that the classical form of the Lucas-Washburn relation is maintained. Note however that the classical Lucas-Washburn relation assumes a fully developed flow at $x = 0$ and $t = 0$. This initial condition is not satisfied in the data presented in Figure 4. As a result, C_V and t_I must be interpreted as parameters that account for inertial effects as well as for variations in viscosity and surface wettability. To delineate the effects of inertia, viscosity variability and wettability from the values of C_V and t_I would require a more complex filling model than eqn S14.

Other filling mechanisms

Although the capillary filling in rectangular nanochannels has been studied in a number of publications,[9-11] the available experimental results are widely scattered. We noted in the main manuscript that our error bars may be interpreted to indicate a slower filling speed (compared to the classical Lucas-Washburn model) in nanoconfinement. Mechanisms for a slower filling speed in nanoconfinement include the formation of electro-viscous layers on channel walls,[9] deformation of the channel walls from capillary pressure,[10] contact angle changes, and the presence of air.[12] The formation of electro-viscous layers on channel walls has previously been used to explain the slow capillary filling rate of demineralized water.[9] However, our experiments use different liquids with different polarities in the same channel, but the results (*i.e.*, the C_V values) are consistent within the reported error bars.

Furthermore, as noted earlier, the liquid-air surface tensions of the fluids vary by a factor of 3.9, but again, we find that the C_V values are consistent within the error bars. Thus, it is unlikely that changes in the contact angle are responsible for the slow filling process. Note also that no bubbles were observed to form in front of liquid-air interface in the inlet part of the nanochannels under the microscope window (see Section 6 below). Moreover, deformation of the channel capillary pressure ($P_C = 2\gamma\cos\theta/h$) cannot explain the results since we would expect the deformation of the channel exposed to each liquid to result in C_V values that vary by a factor of 3.9. Additionally, it has previously been reported that channel deformation results in a slightly *faster* capillary filling.[10] Our manuscript reports the possibility that the viscosities and other bulk properties remain unchanged down to 8 nm confinement.

Section 5: Error analysis for capillary filling

The errors in the values of C_V reported in Table S2 result from uncertainties in the fitted slope of the filling data (see Figure S5), and from the sensitivities of the test fluid properties to the uncertainty of the room temperature, 20 ± 1°C. Uncertainties in the fitted slope are in part due to errors in measuring the filling length. In Figure S5, the measured filling length at a given time is indicated by the black points and blue vertical bars indicate the measurement uncertainty (the standard deviation from 15 repeated runs under the same conditions). The best fit of eqn S14 to the data is show in Figure S5 as a red line. However, two additional fits of eqn S14 can be made when the vertical error bars are considered, as indicated by black dashed line. Thus, the error in the best fit is the maximum of the difference between the red line fit and either dashed line. This error was calculated using Mathematica 11 for each test liquid and the results are listed as uncertainties in the C_V values in Table S2.

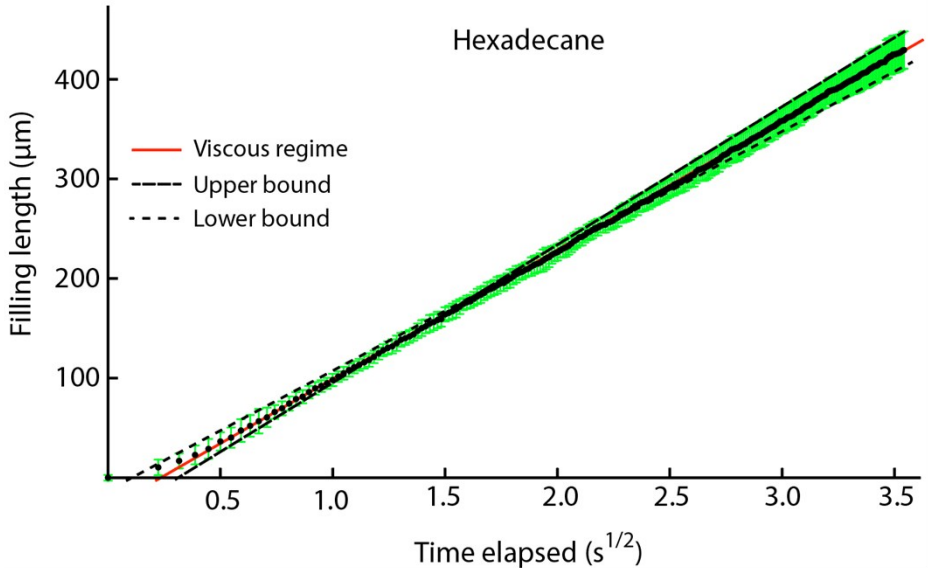

Figure S5. The filling data for hexadecane with filling length (μm) plotted as a function of the square root of time ($s^{0.5}$). Data points shown in black, error bars of the filling length are shown in green, and the best fit to equation (4) is shown in red. Best fits to the error bars are shown as dashed lines.

The room temperature was measured before and after the filling experiments and was found to be steady at 20 ± 1°C. However, the fluid viscosity is sensitive to the temperature. Thus, we evaluated the effects of the room temperature uncertainty on the uncertainty of the fluid properties. Note that the reported viscosities have uncertainties of up to 5%.[3] The approach requires using temperature-dependent expressions for the liquid-air surface tension, and for the liquid dynamic viscosity. Such expressions are readily found in DIPPR[3] for water and for octane, and in Yaws Handbook[4] for hexane and for hexadecane. The uncertainty in a fluid property, δf, can then be determined from

$$\delta f = Max\left[\left|f(T_{room} + \delta T_{room}) - f(T_{room})\right|, \left|f(T_{room} - \delta T_{room}) - f(T_{room})\right|\right] \qquad \text{(S15)}$$

where T_{room} is the room temperature, δT_{room} is the uncertainty in the room temperature, and $f(T)$ is a temperature-dependent function. The results for all six test fluids are listed in Table S1.

Other sources of uncertainty include determination of the contact angle, θ, and of the channel height. Since we cannot directly measure the contact angle in the sub-10 nm channels, we assume that the hydrocarbons are perfectly wetting and use the measured *static* contact angle value of water, as described earlier. As mentioned in the main text, the channel height was measured to be 8.0 ± 0.5 nm and thus has an uncertainty of ± 6.25%. Since the errors in the fluid properties, channel height, and filling length are independent, we may add them using the approach of Taylor[16] to find the overall uncertainty in the value of C_V for each test fluid, δC_V:

$$\delta C_V = \sqrt{\left(\left(\frac{\partial C_V}{\partial \gamma}\right)\delta\gamma\right)^2 + \left(\left(\frac{\partial C_V}{\partial \mu}\right)\delta\mu\right)^2 + \left(\left(\frac{\partial C_V}{\partial h}\right)\delta h\right)^2 + (\delta k)^2} \qquad \text{(S16)}$$

where k is the slope of the best fit to eqn S14, and δX refers to the uncertainty of term X. The results are listed in Table S2. As seen there, values of δC_V for the test fluids indicate that the present experiments do not deviate significantly from the classical Lucas-Washburn relation, *i.e.*, eqn S14 with C_V = 1 and $t_I = 0$. These results suggest that the classical Lucas-Washburn relation may be valid even down to the sub-10 nm scale, after accounting for effects near the nanochannel entrance.

For the hydrocarbons, the modified Lucas-Washburn parameters obtained using the NonlinearModelFit function of Mathematica 11 resulted in R^2 values better than 0.999, indicating a very good fit over the full data range. For the pure water case, the R^2 value was 0.986, indicating a relatively poor fit (see Figure S6).

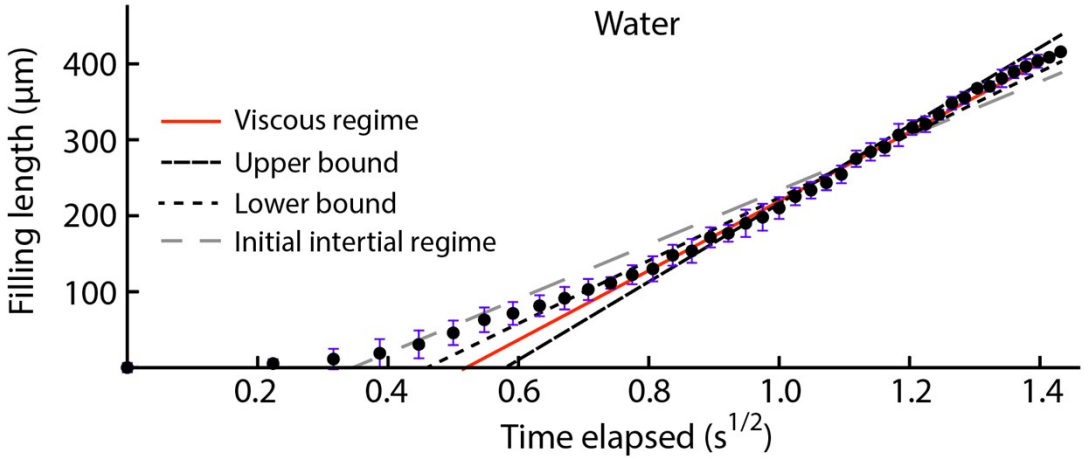

Figure S6. Least-squared fit of the filling data for water with filling length (μm) plotted as a function of time (s). Data points shown in black, error bars of the filling length are shown in blue, and the fit to eqn S14 in the viscous regime is shown in red. The fit uncertainties are shown as dashed black lines. When the initial inertial regime is also considered, the resulting fit is shown as a dashed gray line.

The value for C_V is sensitive to the fitting method applied from the literature. For instance, if the least-square fitting method is applied to the full data range, the water C_V can be as high as 1.31 (± 40%). This fitting method is appropriate when the inertial-dominated period is relatively short and the majority for the filling dynamics is viscous dominated (*i.e.*, follows an x *vs.* $\sqrt{t}$ trend), as for

the hydrocarbons (Figure 4c). For the water case however, the inertial-dominated period persists for a significant period, and it does not make sense to apply the least-square fitting method to the full water data range. Here we prefer the application of fitting to the viscous-dominated regime which allows for the water flow to become fully developed, with the result of $C_V = 0.80$ (± 20%).

Figure S6 shows the least-square-fit of our water experiments to eqn S14, resulting in the C_V value of 1.31 (± 40%). The fit to eqn S14 is shown as a dashed gray line, the data points are in black, and the measurement error bars are in blue. We see that a majority of the fit does not agree with the measurements or the error bars.

The fit can be improved by taking into account the results of Oyarzua *et al.*[17] who claim that the capillary filling for water in nanochannels is initially inertial dominated. The improved fit is shown in Figure S6 as a red line, yielding a water C_V value of 0.80 (± 20%) and an R^2 value better than 0.999 for the data in the range $t > t_I$ (*i.e.*, only fitting to viscous-dominated region).

We take the C_V value of water to be 0.80 (± 20%) since it gives a very good fit to the viscous dominated regime and an R^2 value better than 0.999. The uncertainty of the water C_V value was determined from eqn S16. The result is shown in Figure S6, where the dashed black lines are fits to span the range of the filling length error in the viscous-dominated regime. The uncertainties of the NaCl aqueous solution results were determined in a similar fashion to that described above.

Section 6: Capillary filling video

Movie S1. The video shows the real-time capillary filling of octane in 4-um wide and 8-nm high rectangular channels, as viewed from above. Five channels are shown with the filling occurring from the left to the right. The liquid phase on the left has a slightly pink tone, but is not as bright as the gas phase on the right. Note the ease with which we can see the liquid-gas interface.

We have not directly observed any layering phenomena in our channels under the reported experimental conditions.

Section 7: Debye length calculations for salt concentrations

The Debye length (D) for the NaCl aqueous solution is calculated based on:[20]

$$D = \kappa^{-1} = \left(\frac{N_A e^2}{\varepsilon \varepsilon_0 k_B T} \sum_i z_i^2 c_i^{\infty} \right)^{\frac{-1}{2}}$$

where κ is the Debye-Hückel parameter, $N_A$is Avogadro's number, e is the elementary charge, ε_0 is the permittivity of vacuum, k_B is the Boltzmann constant, T is the temperature, z_i is the valence of the i[th] ion, c_i^{∞} is the concentration of the i[th] ion in bulk, and ε is the dielectric constant of the medium.

For the NaCl aqueous solution at 293 K, it is approximately:[21]

$$\varepsilon = 80 - 10 \times c_i^{\infty}$$

For the concentration of 1.0 M:

$$\frac{N_A e^2}{\varepsilon \varepsilon_0 k_B T} = \frac{6.02 \times 10^{23} \times (1.60 \times 10^{-19})^2}{(80 - 10 \times 1) \times 8.85 \times 10^{-12} \times 1.38 \times 10^{-23} \times 293} = 6.15 \times 10^{15}\, m$$

Therefore the Debye length is:

$$D = \kappa^{-1} = \left(\frac{N_A e^2}{\varepsilon \varepsilon_0 k_B T} \sum_i z_i^2 c_i^{\infty} \right)^{\frac{-1}{2}} = [6.15 \times 10^{15} \times (1 \times 10^3 + 1 \times 10^3)]^{\frac{-1}{2}} = 0.29\, nm$$

Similarly, for the concentration of 0.1 M:

$$\frac{N_A e^2}{\varepsilon \varepsilon_0 k_B T} = \frac{6.02 \times 10^{23} \times (1.60 \times 10^{-19})^2}{(80 - 10 \times 0.1) \times 8.85 \times 10^{-12} \times 1.38 \times 10^{-23} \times 293} = 5.45 \times 10^{15}\, m$$

Therefore the Debye length is:

$$D = \kappa^{-1} = \left(\frac{N_A e^2}{\varepsilon \varepsilon_0 k_B T} \sum_i z_i^2 c_i^{\infty} \right)^{\frac{-1}{2}} = [5.45 \times 10^{15} \times (0.1 \times 10^3 + 0.1 \times 10^3)]^{\frac{-1}{2}} = 0.96\, nm$$

REFERENCES

(1) Duan, C.; Majumdar, A. *Nat. Nanotechnol*. **2010**, *5*, 848-852.
(2) Mao, P.; Han, Jongyoon. *Lab Chip* **2005**, *5*, 837-844.
(3) Design Institute for Physical Property Research/AIChE. *DIPPR Project 801 - Full Version* [Online], **2005**. http://app.knovel.com/hotlink/toc/id:kpDIPPRPF7/dippr-project-801-full/dippr-project-801-full (accessed February 10, 2017)
(4) Yaws, C. L. *Yaws' Thermophysical Properties of Chemicals and Hydrocarbons (Electronic Edition)*. Knovel [Online], **2010**. http://app.knovel.com/hotlink/toc/id:kpYTPCHE02/yaws-thermophysical-properties/yaws-thermophysical-properties (accessed February 10, 2017)
(5) Sumner, A. L.; Menke, E. J.; Dubowski, Y.; Newberg, J. T.; Penner R. M.; Hemminger, J. C.; Wingen, L. M.; Brauers, T.; Finlayson-Pitts, B. J. *Phys. Chem. Chem. Phys.* **2004**, 6, 604-613.
(6) Han, A.; Mondin, G.; Hegelbach, N. G.; de Rooij, N. F.; Staufer, U. *J. Colloid and Interface Sci.* **2006**, *293*, 151-157.
(7) Ichikawa, N.; Hosokawa, K.; Maeda, R. *J. Colloid and Interface Sci.* **2004**, *280*, 155-164.
(8) Oyarzua, E.; Walther, J. H.; Mejia, A.; Zambrano, H. A. *Phys. Chem. Chem. Phys.* **2015**, *17*, 14731-14739.
(9) Tas, N. R.; Haneveld, J.; Jansen, H. V.; Elwenspoek, M.; van den Berg. A. *Appl. Phys. Lett.* **2004**, *85*, 3274-3276.
(10) Haneveld, J.; Tas, N. R.; Brunets, N.; Jansen, H. V.; Elwenspoek, M. *J. Appl. Phys*. **2008**, *104*, 014309.
(11) Kelly S.; Balhoff M. T.; Torres-Verdín, C. *Langmuir*. **2015**, *31*, 2167-2179.
(12) Thamdrup, L. H.; Persson, F.; Bruus, H.; Kristensen, A. Flyvbjerg, H. *Appl. Phys. Lett.* **2007**, *91*, 163505.
(13) Mortensen, N. A.; Kristensen, A. *Appl. Phys. Lett.* **2008**, *92*, 063110.
(14) Phan, V. N.; Nguyen, N. T.; Yang, C.; Joseph, P.; Gué, A. M. *J. Heat Transfer.* **2012**, *134*, 051012.
(15) Asay, D. B.; Kim, S. H. *J. Phys. Chem. B* **2005**, *109*, 16760-16763.
(16) Taylor, J. R. *An Introduction to Error Analysis: The Study of Uncertainties in Physical Measurements*. University Science Books: California, **1997**.
(17) Oyarzua, E.; Walther, J. H.; Mejia, A.; Zambrano, H. A. *Phys. Chem. Chem. Phys.* **2015**, *17*, 14731-14739.
(18) National Physics Laboratory. *Tables of Physical & Chemical Constants (16th edition 1995). 2.2.5 Surface Tensions.* Kaye & Laby [Online], **2005**. http://www.kayelaby.npl.co.uk/general_physics/2_2/2_2_5.html (accessed May 10, 2017).
(19) Kestin, J.; Khalifa, H. E.; Correia, R. J. *J. Phys. Chem. Ref. Data*. **1981**, *10*, 71-87.
(20) Gavish, N.; Promislow, K. *Phys. Rev. E*. **2016**, *91*, 012611.
(21) Schoch, R. B.; Han, J.; Renaud, P. *Rev. Mod. Phys*. **2008**, *80*, 839-883.